

Article

WO₃ Fibers/g-C₃N₄ Z-Scheme Heterostructure Photocatalysts for Simultaneous Oxidation/Reduction of Phenol/Cr (VI) in Aquatic Media

Feidias Bairamis¹ and Ioannis Konstantinou^{1,2,*}¹ Department of Chemistry, University of Ioannina, 45110 Ioannina, Greece; fmpairam@cc.uoi.gr² Institute of Environment and Sustainable Development, University Research Center of Ioannina (URCI), 45110 Ioannina, Greece

* Correspondence: iokonst@uoi.gr; Tel.: +30-26510-08349

Abstract: A sequence of WO₃/g-C₃N₄ composites was synthesized at various % weight ratios (1, 5, 6.5, 8, 10, and 15%) of WO₃ into g-C₃N₄ via electrospinning and wet-mixing method. The prepared photocatalytic materials were characterized by X-ray diffraction (XRD), Fourier transform-infrared (FT-IR) spectroscopy, UV-vis diffuse reflection spectroscopy (DRS), scanning electron microscopy (SEM), N₂ porosimetry and dynamic light scattering (DLS). Electrospun fibers of WO₃ with diameter 250–300 nm was prepared using polyvinylpyrrolidone (PVP) polymer and used for the synthesis of composite WO₃/g-C₃N₄ heterojunction structures. Results showed mesoporous materials with triclinic WO₃ crystal phase, surface areas up to 67.7 m²g⁻¹ and band gaps lower than 2.5 eV confirming the absorption to visible light region. The photocatalytic performance of the prepared photocatalysts were assessed towards the oxidation of phenol and reduction of Cr (VI), in single and binary systems using simulated solar light illumination, that followed first-order kinetics. The WO₃/g-C₃N₄ composites were found to exhibit improved photocatalytic performances compared to the pure WO₃ and g-C₃N₄ with 6.5 wt% WO₃/g-C₃N₄ and 5 wt% WO₃/g-C₃N₄ composites being the most efficient catalysts for the oxidation of phenolics and reduction of Cr (VI), respectively. The improved performance was explained by a Z-scheme photocatalytic mechanism which was proposed based on scavenging experiments and the determination of the corresponding energy levels of valence and conduction bands. The study demonstrated that such composites present interesting photocatalytic properties that can be further expanded to other environmental depollution applications as well as in energy applications.



Citation: Bairamis, F.; Konstantinou, I. WO₃ Fibers/g-C₃N₄ Z-Scheme Heterostructure Photocatalysts for Simultaneous Oxidation/Reduction of Phenol/Cr (VI) in Aquatic Media. *Catalysts* **2021**, *11*, 792. <https://doi.org/10.3390/catal11070792>

Academic Editor: Abel Santos

Received: 4 June 2021

Accepted: 29 June 2021

Published: 29 June 2021

Publisher's Note: MDPI stays neutral with regard to jurisdictional claims in published maps and institutional affiliations.



Copyright: © 2021 by the authors. Licensee MDPI, Basel, Switzerland. This article is an open access article distributed under the terms and conditions of the Creative Commons Attribution (CC BY) license (<https://creativecommons.org/licenses/by/4.0/>).

Keywords: WO₃ fibers; electrospinning; WO₃/g-C₃N₄ composites; phenol/Cr; photocatalytic activity; Z-scheme heterojunction

1. Introduction

Semiconductor based solar light active photocatalysts have received a great attention in environmental remediation and energy production and conversion applications. Among other semiconductors, tungsten oxide (WO₃) is considered as a promising photocatalyst because of its good chemical stability, small band gap (2.4–2.8 eV), non-toxicity and high oxidation ability to degrade persistent organic pollutants. However, the photocatalytic activity of WO₃ is low because of the fast recombination of electron-holes pairs [1–4].

Another promising organic semiconductor, receiving the focus of recent studies on photocatalytic applications, is graphitic carbon nitride (g-C₃N₄). g-C₃N₄ with two-dimensional (2D) nanostructure has relatively narrow band gap (2.7 eV), chemical and thermal (up to 600 °C) stability due to s-triazine ring structure, high resistance in basic and acidic solutions and insolubility in common solvents as water and ethanol. Also, it can be fabricated easily with low-cost precursor compounds like melamine, urea etc. and is non-toxic. However, its photocatalytic efficiency is also limited because of the fast

recombination of photogenerated electron-holes pairs and low ability to generate $\bullet\text{OH}$ radicals [5–7].

In modern strategies for photocatalyst-engineered materials, heterostructuring with a second or a third semiconductor represents one of the most innovative approaches. Heterostructuring can overcome usual limitations of single semiconductors such as low exploitation of solar light, fast electron-hole recombination, inappropriate redox potentials for oxidation or reduction reactions. Direct Z-scheme photocatalytic systems, mimicking natural photosynthesis, represent the most attractive photocatalytic systems because of their advantages such as fast charge separation, suitable band potentials and usually increase light-response [8,9]. There are few works exploring the $\text{WO}_3/\text{g-C}_3\text{N}_4$ heterojunction structure via various methods such as hydrothermal treatment [10–15], wet mixing method [16–22], thermal treatment [23,24] for different purposes such as removal of dyes, degradation of pharmaceuticals and hydrogen production etc.

A simple and low-cost method for the preparation of nanofibers is offered by the electrospinning technique using various polymers (over 200 till now) produced in industrial scale. The (1D) nanofibers presented large surface area to volume ratio and they can weaken the recombination of electron-hole ($\text{h}^+ \text{-e}^-$) better than spherical particles, thus, the photocatalytic activity of a material could improve. The electrospun fibers/materials are being used in different applications such as catalysis, tissue engineering, drug delivery etc [25,26]. According to the current bibliography, a study dealing with the fabrication of WO_3 fibers/ $\text{g-C}_3\text{N}_4$ heterojunction structure combining the electrospinning and wet mixing techniques is lacking. In addition, previously prepared $\text{WO}_3/\text{g-C}_3\text{N}_4$ composites by other methods have not been applied in simultaneous oxido-reduction processes such as the oxidation of organic pollutants and the reduction of toxic heavy metal cations. As a result, the present work deals with the preparation of $\text{g-C}_3\text{N}_4/\text{WO}_3$ composite materials with a range of WO_3 electrospun fibers loadings (up to 15% wt%), their extended physicochemical characterization by a battery of techniques and the evaluation of their photocatalytic performance towards the simultaneous oxidation-reduction processes of phenol and chromium (VI), respectively. Finally, the photocatalytic mechanism taking place in the process was assessed by scavenging and $\bullet\text{OH}$ radical determination, proving a direct Z-scheme system with enhanced performance.

2. Results and Discussion

2.1. Characterization of the Photocatalysts

2.1.1. XRD Patterns and FT-IR Spectra

The XRD patterns for $\text{g-C}_3\text{N}_4$, WO_3 and %WCN composite materials are shown in Figure 1. The characteristic peaks of WO_3 were found at 23.08° , 23.65° , 24.34° , 26.56° , 28.57° , 28.75° , 33.31° , 34.09° , 41.62° , 49.96° , 55.63° which correspond to (002), (020), (200), (120), (112), (022), (202), (004), (400) and (142) planes of the triclinic crystal structure of WO_3 (JCPDS no. 37-1493) [27].

For $\text{g-C}_3\text{N}_4$ two characteristic intense peaks at 13.2° and 27.5° were observed. The peak at $2\theta = 13.2^\circ$ corresponds to the (100) plane of $\text{g-C}_3\text{N}_4$ and it is attributed to the in-plane repetitive and continuous heptazine network. The peak located at $2\theta = 27.5^\circ$ corresponds to the (002) plane of $\text{g-C}_3\text{N}_4$ and it is assigned to the stacking of the conjugated aromatic system. [5–7]. An interplanar distance of aromatic units is calculated to be 3.24 \AA using Bragg's law.

The prepared composite catalysts present closely the same patterns to pristine WO_3 . The diffraction peak intensity of $\text{g-C}_3\text{N}_4$ becomes increasingly lower with increasing the loading of WO_3 , because of the relative lowering content of $\text{g-C}_3\text{N}_4$ as well as the poor crystallinity of $\text{g-C}_3\text{N}_4$ compared to that of WO_3 . In contrast, the diffraction peak intensity of WO_3 becomes more evident with increasing the loading of WO_3 to $\text{g-C}_3\text{N}_4$. The diffraction patterns of $\text{g-C}_3\text{N}_4$ are closely disappeared at 15%wt WO_3 loading, indicating that $\text{g-C}_3\text{N}_4$ has been almost covered by WO_3 fibers. The determined crystal sizes of

the composite materials (12.4–15.3 nm) according to the Scherrer equation presented low variation in respect to pristine WO_3 (12.5 nm) and $\text{g-C}_3\text{N}_4$ (10.8 nm) materials (Table 1).

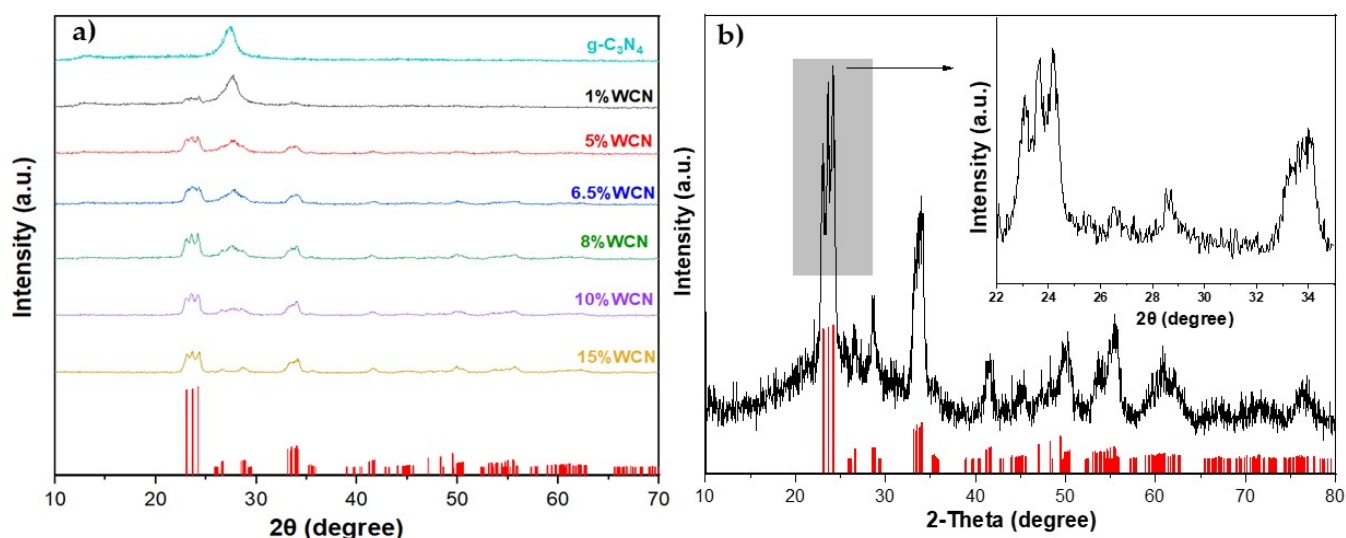


Figure 1. XRD patterns of $\text{g-C}_3\text{N}_4$ and $\text{WO}_3/\text{g-C}_3\text{N}_4$ composite materials (a) and WO_3 fibers (b).

Table 1. Physicochemical properties of prepared catalysts.

Catalyst	Specific Surface Area S_{BET} ($\text{m}^2 \text{g}^{-1}$)	Average Pore Diameter (nm)	V_{TOT} ($\text{cm}^3 \text{g}^{-1}$)	Crystal Size (nm)	Energy Band Gap (eV)	Absorption Edge λ (nm)	DLS Median Diameter (μm)	DLS Modal Diameter (μm)
WO_3 fibers	14.1	10.1	0.035	12.5	2.22	558	0.284	0.282
$\text{g-C}_3\text{N}_4$	10.1	13.1	0.033	10.8	2.51	494	0.220	0.178
1%WCN	51.1	9.8	0.125	15.3	2.49	498	0.434	0.355
5%WCN	58.4	8.9	0.131	13.9	2.47	501	0.335	0.282
6.5%WCN	49.0	9.1	0.112	12.4	2.50	496	0.328	0.282
8%WCN	49.0	9.3	0.113	14.5	2.48	500	0.317	0.282
10%WCN	64.4	8.8	0.142	15.2	2.49	498	0.450	0.447
15%WCN	67.7	8.5	0.144	13.0	2.29	541	0.299	0.282

The FT-IR spectra of the synthesized materials are presented in Figure 2. The peaks of $\text{g-C}_3\text{N}_4$ can be observed at 1539, 1455, 1394, 1316, 1232 cm^{-1} confirming the stretching vibration of C-N(-C)-C or C-NH-C heterocycles. The peak at 804 cm^{-1} is the most characteristic of heptazine rings. The peaks between 3400 and 3000 cm^{-1} are related to the stretching vibration of N-H and stretching vibration mode O-H bond. Also, the peak at 1739 cm^{-1} corresponds to C=N bending vibration and the bending vibration of W-O-W was verified in 500–900 cm^{-1} . The characteristic WO_3 broad peak was more obvious in the materials with the higher WO_3 loadings. Finally, the observed FT-IR spectra of prepared catalysts confirm the formation of composite heterostructures.

2.1.2. Morphology and UV-Vis Diffuse Reflectance

The structural features of all catalysts were also studied by SEM. The WO_3 fibers and the composite materials appeared in Figure 3 and Figure S1. The diameter of fibers varies between 250–300 nm (Figure 3a and Figure S1e). In Figure S1a it is shown the structure of bulk $\text{g-C}_3\text{N}_4$ consisting of stacking sheets. SEM images of composite materials (Figure 1b–d) demonstrated aggregated and disordered WO_3 fibers on $\text{g-C}_3\text{N}_4$ flakes.

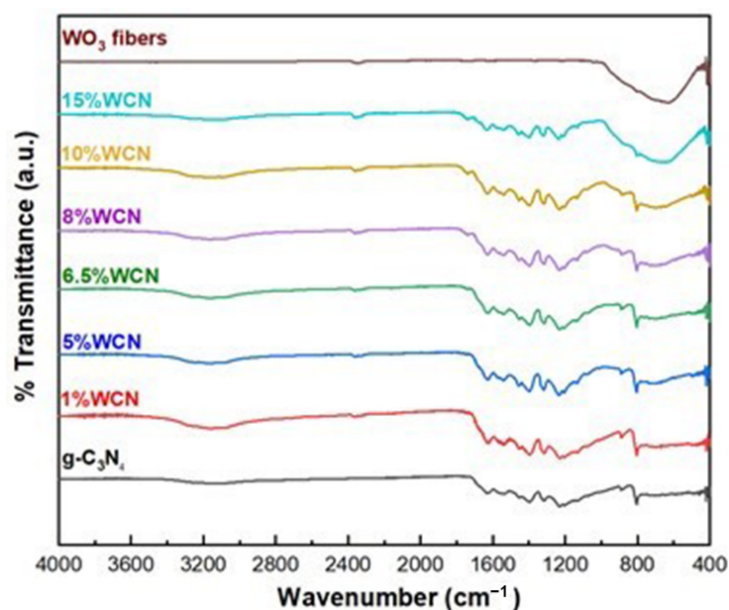


Figure 2. FT-IR spectra of WO_3 fibers, $\text{g-C}_3\text{N}_4$ and composite materials of $\text{WO}_3/\text{g-C}_3\text{N}_4$.

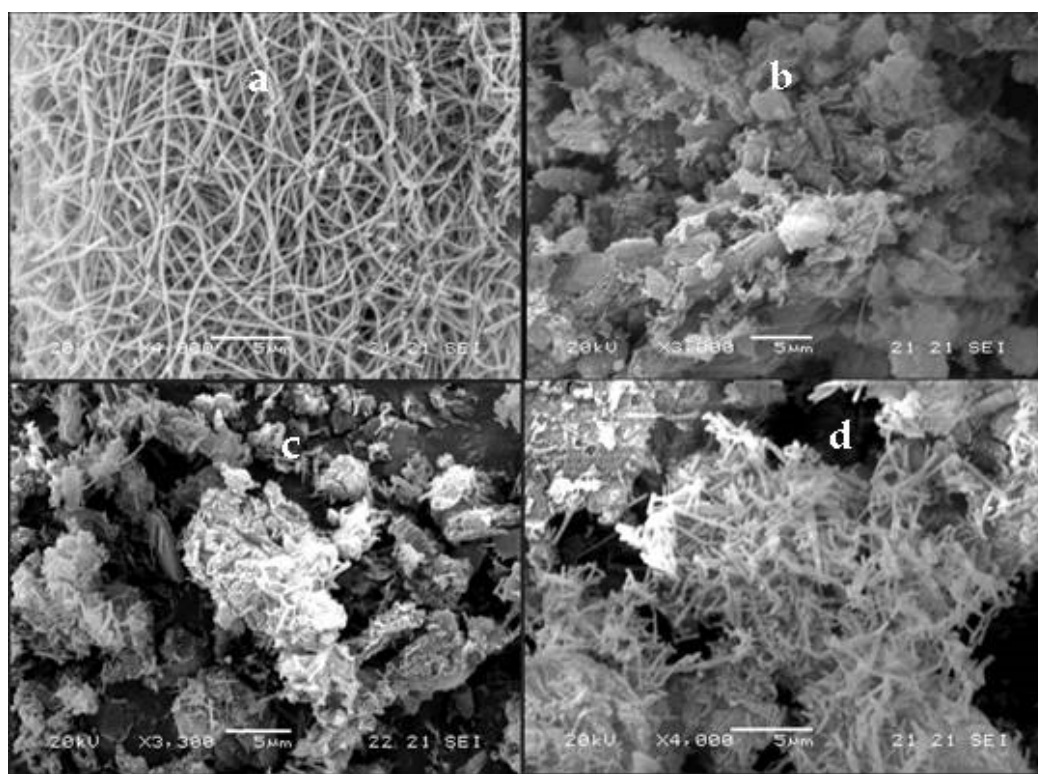


Figure 3. SEM images of electrospun fibers and composite catalysts after calcination (a) WO_3 , (b) 5%WCN (c) 6.5%WCN and (d) 10%WCN.

The nitrogen adsorption-desorption isotherms for the catalysts are displayed in Figure 4 and Figure S2. According to the IUPAC classification, the WO_3 fibers, $\text{g-C}_3\text{N}_4$ and the composite materials are typical mesoporous materials with type IVa adsorption isotherms and H3, H2 (b) (for WO_3 fibers) hysteresis loop type [28]. BET specific surface area for the $\text{WO}_3/\text{g-C}_3\text{N}_4$ composites ranged between $49.0 \text{ m}^2\text{g}^{-1}$ and $67.7 \text{ m}^2\text{g}^{-1}$. The calculated specific surface area, pore diameter and total pore volume of the catalysts are shown in Table 1. Pore volume and surface area of the composites were about 5–7-fold higher

than those of WO_3 and pristine $\text{g-C}_3\text{N}_4$. The reason might be the unordered intercalation of WO_3 fibers between aggregated $\text{g-C}_3\text{N}_4$ flakes.

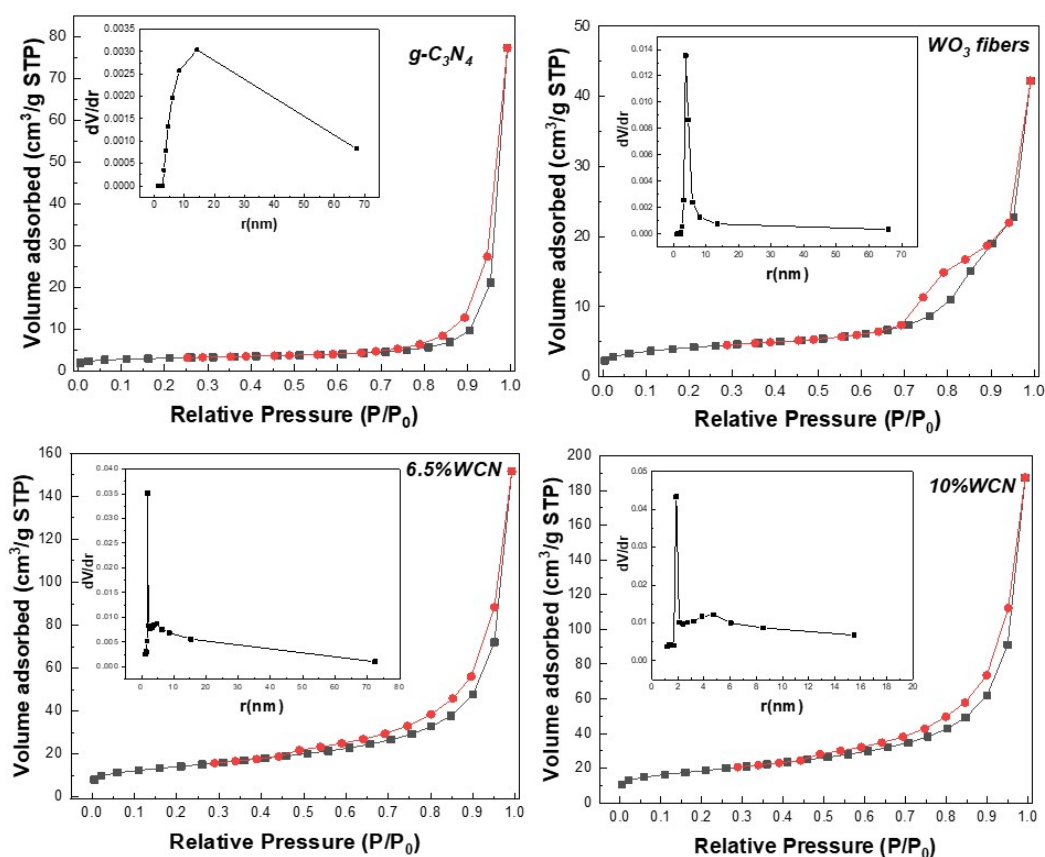


Figure 4. Nitrogen adsorption-desorption isotherms and pore size distributions for the prepared $\text{g-C}_3\text{N}_4$, 5%WCN, 6.5%WCN and 10%WCN.

The optical properties of prepared composite catalysts were investigated by UV-Vis diffuse reflectance spectroscopy. The absorption edge of $\text{g-C}_3\text{N}_4$ sample is determined at 494 nm, and the introduction of WO_3 fibers in $\text{g-C}_3\text{N}_4$ contributed to the increased absorbance of visible-light and red shift. Figure 5 displays the UV-vis absorption spectra of the materials and the energy band gap (E_g) of each photocatalyst determined using the Kubelka-Munk function (Figure 5b and Figure S3). The E_g 's and the absorption edge of the materials are shown in Table 1. The absorption edges of materials varied between 494–558 nm and the energy band gap 2.22–2.51 eV. Calculated E_g values for $\text{g-C}_3\text{N}_4$ and WO_3 agree well with previous reports [14,19,22].

The band edge position of CB and VB of prepared materials was calculated by the following equations:

$$E_{\text{VB}} = X - E_e + 0.5E_g \quad (1)$$

$$E_{\text{CB}} = E_{\text{VB}} - E_g \quad (2)$$

where X is the electronegativity of $\text{g-C}_3\text{N}_4$ (4.67 eV) and WO_3 (6.59 eV); E_e (4.5 eV), which is the energy of free electrons on the hydrogen scale; E_g is the energy band gap of the semiconductors and the E_{VB} and E_{CB} are the potentials for the valence and the conduction band, respectively. According of the above formulas, the E_{VB} and E_{CB} of WO_3 was calculated at 3.2 eV and 0.89 eV while for $\text{g-C}_3\text{N}_4$ the corresponded values were 1.425 eV and -1.085 eV.

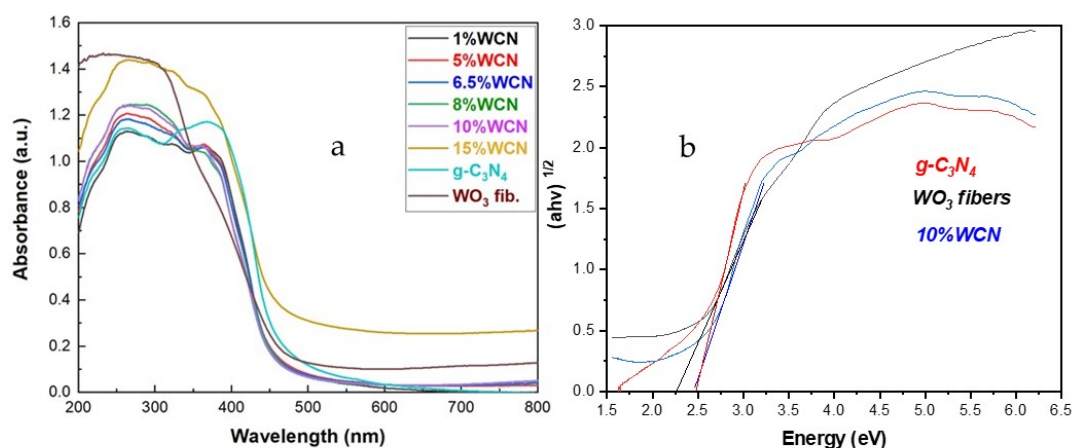


Figure 5. (a) UV-vis absorption spectra of prepared catalysts, (b) Kubelka-Munk plots for WO_3 fibers, $\text{g-C}_3\text{N}_4$ and 10%WCN materials. for indirect band gap semiconductors.

2.2. Photocatalytic Activity

The photocatalytic activity of the prepared catalysts was studied against phenol in single solute systems and against phenol – chromium in binary solute systems. Since it is well-known that phenol photocatalytic degradation proceeds through the formation of various phenolics intermediates, phenolics were also determined in single and binary systems. The results for all photocatalytic experiments are shown in Figure 6, Tables 2 and 3.

Table 2. Photocatalytic degradation kinetics (k , min^{-1} ; $t_{1/2}$, min; R^2) of phenol and phenolic compounds in single system.

Single Catalyst	Phenol			Phenolics		
	k (min^{-1})	$t_{1/2}$ (min)	R^2	k (min^{-1})	$t_{1/2}$ (min)	R^2
WO_3 fibers	0.0007	976.2	0.9959	0.0007	9902.1	0.9593
$\text{g-C}_3\text{N}_4$	0.0018	382.9	0.9889	0.0007	1004.5	0.9501
1%WCN	0.0053	131.7	0.9953	0.0026	265.5	0.9879
5%WCN	0.0081	85.9	0.9936	0.0038	181.4	0.9841
6.5%WCN	0.0095	72.8	0.9975	0.0057	121.6	0.9990
8%WCN	0.0079	87.6	0.9953	0.0022	313.6	0.9079
10%WCN	0.0101	68.4	0.9960	0.0062	112.5	0.9989
15%WCN	0.0042	166.2	0.9888	0.0011	613.4	0.9900

Table 3. Photocatalytic degradation kinetics (k , min^{-1} ; $t_{1/2}$, min; R^2) of phenol, phenolics and Cr (VI) in binary system.

Binary Catalyst	Phenol			Phenolics			Cr (VI)		
	k (min^{-1})	$t_{1/2}$ (min)	R^2	k (min^{-1})	$t_{1/2}$ (min)	R^2	k (min^{-1})	$t_{1/2}$ (min)	R^2
WO_3 fibers	0.0043	163.1	0.9972	0.0064	109.1	0.9970	0.0019	362.9	0.9685
$\text{g-C}_3\text{N}_4$	0.0024	294.9	0.8700	0.0060	115.7	0.9904	0.0025	278.3	0.9633
1%WCN	0.0095	73.1	0.9911	0.0288	24.1	0.9774	0.0098	70.9	0.9554
5%WCN	0.0165	41.9	0.9791	0.0454	15.2	0.9790	0.0169	41.1	0.9380
6.5%WCN	0.0122	56.8	0.9977	0.0471	14.7	0.9889	0.0155	44.6	0.9714
8%WCN	0.0045	152.6	0.9798	0.0196	35.4	0.9938	0.0057	120.9	0.9345
10%WCN	0.0090	76.9	0.9959	0.0331	20.9	0.9607	0.0096	71.1	0.9685
15%WCN	0.0125	55.3	0.9935	0.0248	27.9	0.9886	0.0087	79.9	0.9582
6.5%WCN _p	-	-	-	0.0448	15.5	0.9818	0.0117	59.2	0.9836

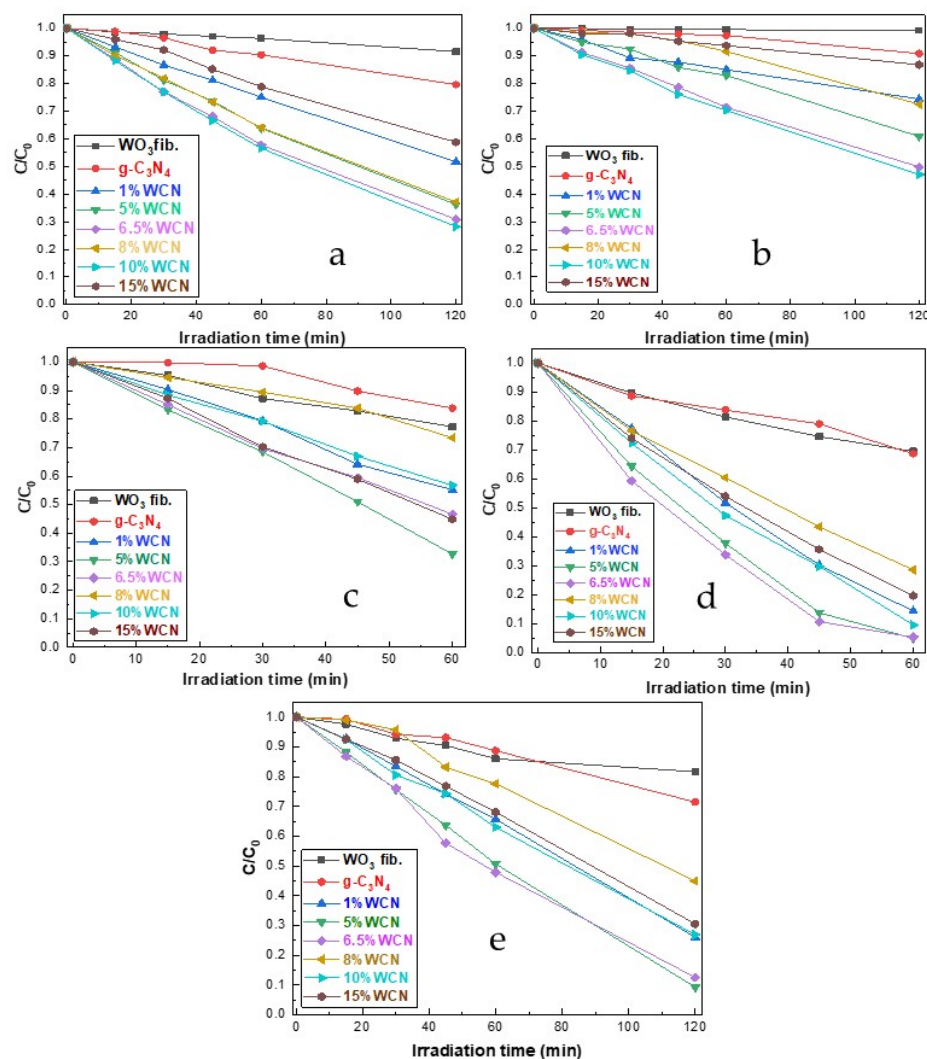


Figure 6. Photocatalytic degradation kinetics of phenol (a) and phenolics (b) in single system; and phenol (c), phenolics (d) and Cr (VI) (e) in binary system with the presence of synthesized catalysts under simulated solar light irradiation.

The first order kinetics for phenol and phenolics photocatalytic degradation in single systems increase according to the following trends: $k_{10\%WCN} > k_{6.5\%WCN} > k_{5\%WCN} > k_{8\%WCN} > k_{1\%WCN} > k_{15\%WCN} > k_{g-C_3N_4} > k_{WO_3 \text{ fibers}}$; and $k_{10\%WCN} > k_{6.5\%WCN} > k_{5\%WCN} > k_{1\%WCN} > k_{8\%WCN} > k_{15\%WCN} > k_{g-C_3N_4} > k_{WO_3 \text{ fibers}}$, respectively. Moreover, the trends in binary systems for phenol, phenolic compounds degradation and chromium (VI) reduction followed the series: $k_{5\%WCN} > k_{15\%WCN} > k_{6.5\%WCN} > k_{1\%WCN} > k_{10\%WCN} > k_{8\%WCN} > k_{WO_3 \text{ fibers}} > k_{g-C_3N_4}$ (for phenol); $k_{6.5\%WCN} > k_{5\%WCN} > k_{10\%WCN} > k_{1\%WCN} > k_{15\%WCN} > k_{8\%WCN} > k_{WO_3 \text{ fibers}} > k_{g-C_3N_4}$ and (for phenolics); and $k_{5\%WCN} > k_{6.5\%WCN} > k_{1\%WCN} > k_{10\%WCN} > k_{15\%WCN} > k_{8\%WCN} > k_{g-C_3N_4} > k_{WO_3 \text{ fibers}}$ (for Cr (VI)). Also, the kinetics for degradation of phenolics and chromium (VI) reduction using the catalyst prepared with commercial WO_3 particles ($6.5\%WCN_p$) in binary systems were slightly slower compared with $6.5\%WCN$ catalyst (phenolics; $k_{6.5\%WCN} > k_{6.5\%WCN_p}$ and Cr (VI); $k_{6.5\%WCN} > k_{6.5\%WCN_p}$). Finally, comparing the kinetics of phenol and phenolic compounds for the different composite catalysts for single and binary systems showed that the kinetics are faster in binary systems than the single systems.

2.3. Photocatalytic Mechanism for the $WO_3/g-C_3N_4$ Composite Catalysts

In order to investigate the photocatalytic mechanism, a series of photocatalytic experiments in the presence scavengers have been performed. Isopropanol (IPA), triethanolamine

(TEOA), sodium azide (NaN_3), and superoxide dismutase (SOD) can act as scavengers of $\bullet\text{OH}$, h^+ , singlet oxygen ($^1\text{O}_2$) and $\bullet\text{OH}$; $\text{O}_2^{\bullet-}$, respectively. Figure 7 shows the effects of scavengers on the photocatalytic kinetics for 10%WCN catalyst. After adding, IPA, NaN_3 and SOD the degradation rate constant for phenol was decreased by 68%, 71% and 57%, respectively. When TEOA was added, the photocatalytic efficiency was significantly reduced by 92%. The degradation kinetics of phenol in the presence of IPA and NaN_3 are almost similar, indicating that $^1\text{O}_2$ doesn't display a significant role on the photocatalytic process. In addition, the high inhibition in the presence of SOD denoted also the formation of $\text{O}_2^{\bullet-}$ and the effective charge separation with the electrons being captured by the molecular oxygen.

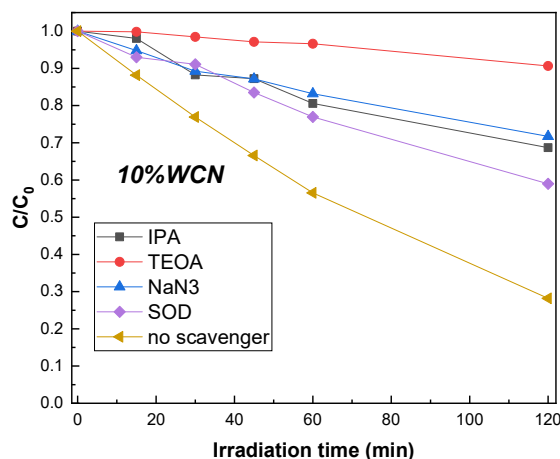


Figure 7. Scavenging experiments of phenol photocatalytic degradation under simulated solar light irradiation and the presence of 10%WCN.

Moreover, based on the inhibition in the presence of TEOA direct hole oxidation might take also place, according also to the oxidation potential of phenol (0.86 V vs NHE). Finally, according to fluorescence (FL) measurements after 120 min of irradiation, the concentrations of $\bullet\text{OH}$ for the catalysts $\text{g-C}_3\text{N}_4$, WO_3 and 10%WCN were calculated at 0.4 μM , 1.6 μM and 2.6 μM , respectively. Overall, the presence of scavengers leads to decreased degradation efficiency indicating that the major active species involved in the photocatalytic reaction are $\bullet\text{OH}$, h^+ and $\text{O}_2^{\bullet-}$.

If a type II heterojunction (Figure 8) is considered for the composite catalysts, the photogenerated electrons would transport from the CB of $\text{g-C}_3\text{N}_4$ to the CB of WO_3 and the holes would form from the VB of WO_3 to VB of $\text{g-C}_3\text{N}_4$. However, in this case scenario, the accumulated electrons in the CB of WO_3 couldn't reduce O_2 to generate $\bullet\text{O}_2^-$ radicals (WO_3 $E_{\text{CB}} = +0.89$ eV; $\text{O}_2/\text{O}_2^{\bullet-}$ (−0.33 eV vs NHE)) and the collected holes couldn't oxidize OH^- or H_2O to form $\bullet\text{OH}$ ($\text{g-C}_3\text{N}_4$, $E_{\text{VB}} = +1.425$ eV; $\text{OH}^-/\bullet\text{OH}$ (+1.99 eV vs NHE); $\text{H}_2\text{O}/\bullet\text{OH}$ (+2.4 eV vs NHE)). As a result, type II photocatalytic mechanism is excluded. On the contrary, the formation and the participation of $\bullet\text{OH}$ and $\text{O}_2^{\bullet-}$ in the photocatalytic degradation based on the scavenging experiments and fluorescence measurements as well as the determined band edge positions for WO_3 and $\text{g-C}_3\text{N}_4$ demonstrate a Z-scheme mechanism (Figure 9).

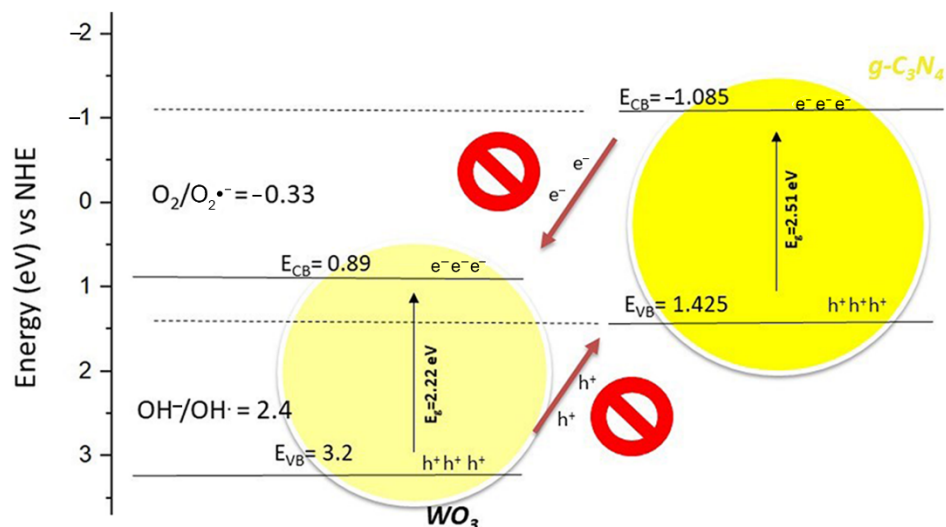


Figure 8. Illustration of improbable type-II photocatalytic mechanism for the composite materials.

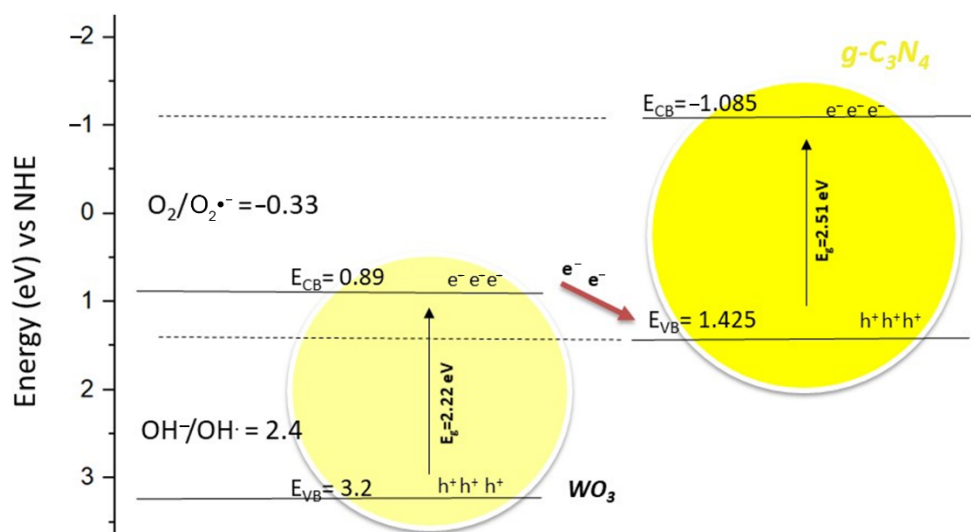


Figure 9. Proposed Z-scheme photocatalytic mechanism for the composite materials.

The gap between the CB $g\text{-C}_3\text{N}_4$ and the CB WO_3 is about 1.98 eV, which is four times larger than the gap between the VB of $g\text{-C}_3\text{N}_4$ and the CB of WO_3 (0.53 eV), leading the electrons from CB of WO_3 to transfer to the VB of $g\text{-C}_3\text{N}_4$. Consequently, the holes and the electrons will gather in the VB of WO_3 and the CB of $g\text{-C}_3\text{N}_4$, respectively. The corresponding band potentials matched well with the production of the reactive species determined as well as on the oxidation of phenol and reduction of chromium species. In this way, the heterojunction will exhibit strong oxidize and reduction capability, representing an interesting system for both oxido-reductive applications.

2.4. Recyclability of the Composite Catalyst

In order to investigate the recyclability of the synthesized photocatalysts, the photocatalytic activity against phenolics in binary systems using one of the most efficient photocatalyst 6.5%WCN was studied for three consecutive cycles. According to the experimental results (Figure S4) the apparent reaction constants determined for the first, second and third catalytic cycle were 0.0469 min^{-1} , 0.0460 min^{-1} and 0.0433 min^{-1} for the degradation of phenolics, respectively. A loss of 8% of its catalytic performance was recorded after the third cycle. In combination with SEM (Figure S5) and FT-IR (Figure S6)

analysis, a high stability of the catalyst can be suggested taking into account also potential losses during the catalyst recovery process.

3. Materials and Methods

3.1. Materials and Chemicals

Poly-vinyl (pyrrolidone) (PVP, Mw: 1.300.000 gmol^{-1}), ammonium metatungstate hydrate (AMH, Mw: 2956.30 gmol^{-1}), melamine (Mw: 126.12 gmol^{-1}), sodium carbonate (Na_2CO_3 , Mw: 105.99 gmol^{-1}), potassium dichromate (KCr_2O_7 , Mw: 294.18 gmol^{-1}) and commercial tungsten (VI) oxide (WO_3 , Mw: 231.84 gmol^{-1} , particles size < 100 nm) were obtained from Sigma Aldrich (St. Louis, MO, USA). Methanol (MeOH), sulfuric acid >95% (H_2SO_4), methanol HPLC grade (MeOH, Mw: 32.04 gmol^{-1}) and water HPLC grade (Mw: 18.02 gmol^{-1}) were supplied by Fischer Scientific (Loughborough, Leics, UK). Phenol (Mw: 94.11 gmol^{-1}) and Folin–Ciocalteu’s phenol reagent were purchased by Merck KGaA (Darmstadt, Germany). Terephthalic acid (TA) (98%) was purchased from Sigma-Aldrich, (St. Louis, MO, USA). Ethanol 99.8% (EtOH, Mw: 46.06 gmol^{-1}) and 1,5-diphenyl carbazide 97+% (Fw: 242.98) were obtained from Acros Organics (Geel, Belgium) and Alfa Aesar (Kandel, Germany), respectively. Bi-distilled water was used throughout the experimental procedures of the study.

3.2. Preparation of Electrospun WO_3 Fibers, $g\text{-C}_3\text{N}_4$ and Composite Materials $\text{WO}_3/g\text{-C}_3\text{N}_4$

The WO_3 fibers were synthesized in a typical horizontal set up of electrospinning apparatus using a grounded collecting metal plate. Firstly, a PVP (0.2 g) solution in methanol (2.5 mL) and a second solution of AMH (0.125 g) in bi-distilled water (1.25 mL) were prepared and stirred by vortex to ensure complete dissolution. Then, AMH solution was transferred to PVP solution and stirred again by vortex until to achieve a homogeneous solution. Afterwards, the final mixture was added into a plastic syringe and placed in the syringe-pump (Holliston, Ma, USA). Electrospinning process was carried out at room temperature, kept between 27–30 °C, with a relative humidity of 32–35% according to previously selected conditions [29]. Moreover, the applied voltage was set at 20 kV, the distance between the tip and the collector was 15 cm and the feed rate of solution was 1 mLh^{-1} . The fabricated fibers were calcinated at 500 °C for 3 h with a heating rate of 2 °C min^{-1} . The $g\text{-C}_3\text{N}_4$ powder was synthesized using melamine as precursor compound. The melamine was calcinated in air at 550 °C for 4 h with a heating rate of 10 °C min^{-1} in a covered quartz crucible, which was whole wrapped with aluminum foil, then allowed to cool down naturally. The obtained yellow color solid was ground well into a fine powder in an agate mortar. The $\text{WO}_3/g\text{-C}_3\text{N}_4$ composite catalysts were synthesized by the wet mixing method. Each time, the as-prepared catalyst powders were added in 50 mL of bi-distilled water and the resulting suspension was stirred for 2 h and heated until dryness. The collected catalysts were calcinated at 520 °C for 2 h with a heating rate of 5 °C min^{-1} . The as-prepared catalysts were named as 1%WCN, 5%WCN, 6.5%WCN, 8%WCN, 10%WCN, 15%WCN, respectively to the %weight of WO_3 . For comparison purposes, a composite catalyst with WO_3 particles and 6.5% weight of WO_3 was also synthesized according to the previous methodology and named as 6.5%WCN_p.

3.3. Characterization

The X-ray diffraction (XRD) patterns of the fabricated catalysts were recorded using a Bruker Advance D8 instrument (Billerica, MA, USA) working with Cu-K_α ($\lambda = 1.5406 \text{ \AA}$) radiation. Diffractograms were scanned from 2θ 10° to 70° in steps of 0.02° and a rate 0.01 ° θ s^{-1} . The patterns were assigned to crystal phases with the use of the International Center for Diffraction Data (ICDD). The morphology and the size of fibers were observed by scanning electron microscopy (SEM) using a JEOL JSM 5600 instrument (Tokyo, Japan) working at 20 kV.

Nitrogen adsorption-desorption isotherms were measured using a Quantachrome Autosorb-1 instrument (Bounton Beach, FL, USA) at 77K. The prepared catalysts ($\approx 80 \text{ mg}$)

were degassed at 423 K for 3 h. Brunauer-Emmet-Teller (BET) method was used at relative pressure between 0.05–0.3, in order to calculate the specific surface area (SSA) of each material. Adsorbed amount of nitrogen at relative pressure $P/P_0 = 0.95$ was used in order to calculate the total pore volume (V_{TOT}). The BJH (Barrett, Joyner and Halenda) method was used to determine the pore size distribution (PSD) of the photocatalysts.

A Shimadzu SALD-2300 laser diffraction particle size analyzer (Kyoto, Japan) working with dynamic light scattering (DLS) mode was used for catalysts' hydrodynamic particle size measurements. Suspensions of the catalysts were prepared by stirring for 2.5 h.

3.4. Spectroscopy Measurements

Attenuated Total Reflectance-Fourier Transform Infrared spectra (ATR-FT-IR) were obtained by a Shimadzu IR Spirit QATR-S (Kyoto, Japan). The fabricated photocatalysts were scanned in the range 4000–400 min^{-1} .

Diffuse reflectance spectra (DRS) of the fabricated catalysts were carried out on a Shimadzu 2600 spectrophotometer bearing an IRS-2600 integrating sphere (Kyoto, Japan) in the wavelength range of 200–800 nm at room temperature using BaSO_4 (Nacalai Tesque, extra pure reagent, Kyoto, Japan), as a reference sample.

3.5. Determination of $\bullet\text{OH}$ Radicals by Fluorescence Measurements

The formation of hydroxyl radicals was studied using terephthalic acid (TA) method. An aqueous solution (100 mL) of NaOH (2×10^{-3} M, 99% Riedel-de Haën, Seelze, Germany) and TA (5×10^{-4} M) was prepared and then 10 mg of the photocatalyst powder was added and the suspension was placed in the photocatalytic reactor [30,31] following the same irradiation conditions followed in the photocatalytic experiments.

3.6. Evaluation of Photocatalytic Performance

The photocatalytic activity was evaluated towards the oxidation of phenol and the reduction of chromium. The solar simulator apparatus Suntest XLS+ (Atlas, Germany) disposing a xenon lamp 2.2kW jacked with special 290 nm cut-off glass filter was used for the photocatalytic experiments. The irradiation intensity was maintained at 500 Wm^{-2} during the experiments. The set-up of the photocatalytic reactor was described in previous studies [29,30]. For the photocatalytic experiments, 100 mL of phenol (10 mgL^{-1}) solution were loaded in Pyrex glass reactor thermostated at ambient conditions ($\approx 20^\circ\text{C}$), by water circuit flowing in the double-skin of the reactor and air-flow, under continuous stirring. The molar ratio of phenol: Cr (VI) was set to 1:5 while the pH of solutions was adjusted by H_2SO_4 at pH = 2. Before illumination the suspension was magnetically stirred for 30 min to ensure the establishment of adsorption-desorption equilibrium onto the catalyst surface. The samples taken at different time intervals were filtered through 0.22 μm PTFE syringe filters. The concentrations of Cr (VI) and phenolics were determined by the diphenyl-carbazide and Folin-Ciocalteu reagent, respectively. The samples were analyzed by UV-Vis-spectroscopy (Jasco-V630, Tokyo, Japan) measuring the absorbance at the characteristic wavelength of 540 nm for Cr (VI) and 765 nm for phenolics. Determination of phenol concentration was carried out by high-performance liquid chromatography (HPLC) (Schimadzu, LC 10AD, Diode Array Detector SPD-M10A, Degasser DGU-14A). The mobile phase was a mixture of HPLC grade water (50%) and MeOH (50%). The column oven (Schimadzu, CTO-10A) was set at 40 $^\circ\text{C}$.

4. Conclusions

In summary, g- $\text{C}_3\text{N}_4/\text{WO}_3$ composite catalysts (up to 15% wt of WO_3) have been successfully prepared combining the electrospinning process and the wet mixing method. The composite materials presented mainly triclinic crystal phase of WO_3 , mesoporosity and increased response to visible light irradiation. The materials presented increased efficiency for the both oxidation and reduction processes as determined towards the oxidation of phenol and reduction of Cr (VI) as well as high stability. Photocatalytic efficiencies of

materials are better in binary systems than the single systems. A Z-scheme photocatalytic mechanism was proposed for the composites make them promising systems for versatile photocatalytic application in environmental remediation and energy conversion. The ease preparation in large quantities constitute another advantage for their applications.

Supplementary Materials: The following are available online at <https://www.mdpi.com/article/10.3390/catal11070792/s1>. Figure S1: SEM images of electrospun fibers and composite catalysts after calcination (a) g-C₃N₄, (b) 1%WCN (c) 8%WCN, (d) 15%WCN and (e) WO₃ fibers. Figure S2: Nitrogen adsorption-desorption isotherms and pore size distributions for the prepared materials 1%WCN, 5%WCN, 8%WCN and 15%WCN. Figure S3: Kübelka-Munk plots for 1%WCN, 5%WCN, 6.5%WCN, 8%WCN and 15%WCN materials. Figure S4: Reusability performance of 6.5%WCN catalyst. Figure S5: SEM image of catalyst 6.5%WCN after three photocatalytic cycle. Figure S6: FT-IR spectra of composite material 6.5%WCN after the third photocatalytic cycle.

Author Contributions: Conceptualization, I.K.; methodology, F.B. and I.K.; formal analysis, F.B.; investigation, F.B.; resources, I.K.; data curation, F.B.; writing—original draft preparation, F.B. and I.K.; writing—review and editing, F.B. and I.K.; visualization, F.B.; supervision, I.K.; project administration, F.B.; funding acquisition, I.K. All authors have read and agreed to the published version of the manuscript.

Funding: This research work was funded by the Hellenic foundation for Research and Innovation (HFRI) under the HFRI PhD fellowship grant (Fellowship number: 269), project number: 82697.

Data Availability Statement: Data are contained within the article and the supporting information file.

Acknowledgments: The authors acknowledge the access in XRD and SEM units of the University of Ioannina. The authors would like to thank T. Vaimakis and D. Petrakis for their long-term collaboration in the Laboratory of Industrial Chemistry, Dept. of Chemistry, University of Ioannina.

Conflicts of Interest: The authors declare no conflict of interest.

References

1. Chen, S.; Hu, Y.; Meng, S.; Fu, X. Study on the separation mechanisms of photogenerated electrons and holes for composite photocatalysts g-C₃N₄-WO₃. *Appl. Catal. B Environ.* **2014**, *150–151*, 564–573. [CrossRef]
2. Cui, L.; Ding, X.; Wang, Y.; Shi, H.; Huang, L.; Kang, S. Facile Preparation of Z-scheme WO₃/g-C₃N₄ Composite Photocatalyst with Enhanced Photocatalytic Performance under Visible Light. *Appl. Surf. Sci.* **2017**, *391*, 202–210. [CrossRef]
3. Jin, Z.; Murakami, N.; Tsubota, T.; Ohno, T. Complete oxidation of acetaldehyde over a composite photocatalyst of graphitic carbon nitride and tungsten (VI) oxide under visible-light irradiation. *Appl. Catal. B Environ.* **2014**, *150–151*, 479–485. [CrossRef]
4. Yan, H.; Zhu, Z.; Long, Y.; Li, W. Single-source-precursor-assisted synthesis of porous WO₃/g-C₃N₄ with enhanced photocatalytic property. *Colloids Surf. A* **2019**, *582*, 123857. [CrossRef]
5. Mamba, G.; Mishra, A.K. Graphitic carbon nitride (g-C₃N₄) nanocomposites: A new and exciting generation of visible light driven photocatalysts for environmental pollution remediation. *Appl. Catal. B Environ.* **2016**, *198*, 347–377. [CrossRef]
6. Wang, Y.; Wang, X.; Antonietti, M. Polymeric graphitic carbon nitride as a heterogeneous organocatalyst: From photochemistry to multipurpose catalysis to sustainable chemistry. *Angew. Chem. Int. Ed.* **2012**, *51*, 68–89. [CrossRef]
7. Zhao, J.; Ji, Z.; Shen, X.; Zhou, H.; Ma, L. Facile synthesis of WO₃ nanorods/g-C₃N₄ composites with enhanced photocatalytic activity. *Ceram. Int.* **2015**, *41*, 5600–5606. [CrossRef]
8. Zhu, Y.; Ameyama, K.; Anderson, P.M.; Beyerlein, I.J.; Gao, H.; Kim, H.S.; Lavernia, E.; Mathaudhu, S.; Mughrabi, H.; Ritchie, R.O.; et al. Heterostructured materials: Superior properties from hetero-zone interaction. *Mater. Res. Lett.* **2021**, *9*, 1–31. [CrossRef]
9. Low, J.; Jiang, C.; Cheng, B.; Wageh, S.; Al-Ghamdi, A.A.; Yu, J. A Review of Direct Z-Scheme Photocatalysts. *Small Methods* **2017**, *1700080*. [CrossRef]
10. Xiao, T.; Tang, Z.; Yang, Y.; Tang, L.; Zhou, Y.; Zou, Z. In situ construction of hierarchical WO₃/g-C₃N₄ composite hollow microspheres as a Z-scheme photocatalyst for the degradation of antibiotics. *Appl. Catal. B Environ.* **2018**, *220*, 417–428. [CrossRef]
11. Priya, A.; Senthil, R.A.; Selvi, A.; Arunachalam, P.; Senthil, K.C.K.; Madhavan, J.; Boddula, R.; Pothu, R.; Al-Mayouf, A.M. A study of photocatalytic and photoelectrochemical activity of as-synthesized WO₃/g-C₃N₄ composite photocatalysts for AO7 degradation. *Mater. Sci. Energy Technol.* **2020**, *3*, 43–50. [CrossRef]
12. Zhang, X.; Wang, X.; Meng, J.; Liu, Y.; Ren, M.; Guo, Y.; Yang, Y. Robust Z-scheme g-C₃N₄/WO₃ heterojunction photocatalysts with morphology control of WO₃ for efficient degradation of phenolic pollutants. *Sep. Purif. Technol.* **2021**, *255*, 117693. [CrossRef]
13. Han, X.; Xu, D.; An, L.; Hou, C.; Li, Y.; Zhang, Q.; Wang, H. WO₃/g-C₃N₄ two-dimensional composites for visible-light driven photocatalytic hydrogen production. *Int. J. Hydrog. Energy* **2018**, *43*, 4845–4855. [CrossRef]

14. Zhu, W.; Sun, F.; Goei, R.; Zhou, Y. Construction of WO₃-g-C₃N₄ composites as efficient photocatalysts for pharmaceutical degradation under visible light. *Catal. Sci. Technol.* **2017**, *7*, 2591–2600. [[CrossRef](#)]
15. Sun, X.Y.; Zhang, F.J.; Kong, C. Porous g-C₃N₄/WO₃ photocatalyst prepared by simple calcination for efficient hydrogen generation under visible light. *Colloids Surf. A Physicochem. Eng. Asp.* **2020**, *594*, 124653. [[CrossRef](#)]
16. Chai, B.; Liu, C.; Yan, J.; Ren, Z.; Wang, Z.-J. In-situ synthesis of WO₃ nanoplates anchored on g-C₃N₄ Z-scheme photocatalysts for significantly enhanced photocatalytic activity. *Appl. Surf. Sci.* **2018**, *448*, 1–8. [[CrossRef](#)]
17. Wang, P.; Lu, N.; Su, Y.; Liu, N.; Yu, H.; Li, J.; Wu, Y. Fabrication of WO₃@g-C₃N₄ with core@shell nanostructure for enhanced photocatalytic degradation activity under visible light. *Appl. Surf. Sci.* **2017**, *423*, 197–204. [[CrossRef](#)]
18. Singh, J.; Arora, A.; Basu, S. Synthesis of coral like WO₃/g-C₃N₄ nanocomposites for the removal of hazardous dyes under visible light. *J. Alloys Compd.* **2019**, *808*, 151734. [[CrossRef](#)]
19. Cadan, F.M.; Ribeiro, C.; Azevedo, E.B. Improving g-C₃N₄:WO₃ Z-scheme photocatalytic performance under visible light by multivariate optimization of g-C₃N₄ synthesis. *Appl. Surf. Sci.* **2021**, *537*, 147904. [[CrossRef](#)]
20. Jing, H.; Ou, R.; Yu, H.; Zhao, Y.; Lu, Y.; Huo, M.; Huo, H.; Wang, X. Engineering of g-C₃N₄ nanoparticles/WO₃ hollow microspheres photocatalyst with Z-scheme heterostructure for boosting tetracycline hydrochloride degradation. *Sep. Purif. Technol.* **2021**, *255*, 117646. [[CrossRef](#)]
21. Liu, X.; Jin, A.; Jia, Y.; Xia, T.; Deng, C.; Zhu, M.; Chen, C.; Chen, X. Synergy of adsorption and visible-light photocatalytic degradation of methylene blue by a bifunctional Z-scheme heterojunction of WO₃/g-C₃N₄. *Appl. Surf. Sci.* **2017**, *405*, 359–371. [[CrossRef](#)]
22. Yao, J.; Zhang, M.; Yin, H.; Luo, Y.; Liu, X. Improved photocatalytic activity of WO₃/C₃N₄: By constructing an anchoring morphology with a Z-scheme band structure. *Solid State Sci.* **2019**, *95*, 105926. [[CrossRef](#)]
23. Chang, F.; Zheng, J.; Wu, F.; Wang, X.; Deng, B. Binary composites WO₃/g-C₃N₄ in porous morphology: Facile construction, characterization, and reinforced visible light photocatalytic activity. *Colloids Surf. A Physicochem. Eng. Asp.* **2019**, *563*, 11–21. [[CrossRef](#)]
24. Zhang, F.; Huang, L.; Ding, P.; Wang, C.; Wang, Q.; Wang, H.; Li, Y.; Xu, H.; Li, H. One-step oxygen vacancy engineering of WO₃-x/2D g-C₃N₄ heterostructure: Triple effects for sustaining photoactivity. *J. Alloys Compd.* **2019**, *795*, 426–435. [[CrossRef](#)]
25. Bhardwaj, N.; Kundu, S.C. Electrospinning: A fascinating fiber fabrication technique. *Biotechnol. Adv.* **2010**, *28*, 325–347. [[CrossRef](#)] [[PubMed](#)]
26. Dong, Z.; Kennedy, S.J.; Wu, Y. Electrospinning materials for energy-related applications and devices. *J. Power Sources* **2011**, *196*, 4886–4904. [[CrossRef](#)]
27. Feng, M.; Liu, Y.; Zhao, Z.; Huang, H.; Peng, Z. The preparation of Fe doped triclinic-hexagonal phase heterojunction WO₃ film and its enhanced photocatalytic reduction of Cr (VI). *Mater. Res. Bull.* **2019**, *109*, 168–174. [[CrossRef](#)]
28. Thommes, M.; Kaneko, K.; Neimark, A.V.; Olivier, J.P.; Rodriguez-Reinoso, F.; Rouquerol, J.; Sing, K.S.W. Physisorption of gases, with special reference to the evaluation of surface area and pore size distribution (IUPAC Technical Report). *Pure Appl. Chem.* **2015**, *87*, 1051–1069. [[CrossRef](#)]
29. Bairamis, F.; Konstantinou, I.; Petrakis, D.; Vaimakis, T. Enhanced Performance of Electrospun Nanofibrous TiO₂/g-C₃N₄ Photocatalyst in Photocatalytic Degradation of Methylene Blue. *Catalysts* **2019**, *9*, 880. [[CrossRef](#)]
30. Giannakas, A.; Bairamis, F.; Papakostas, I.; Zerva, T.; Konstantinou, I. Evaluation of TiO₂/V₂O₅ and N,F-doped-TiO₂/V₂O₅ nanocomposite photocatalysts toward reduction of Cr(VI) and oxidation reactions by •OH radicals. *J. Ind. Eng. Chem.* **2018**, *65*, 370–379. [[CrossRef](#)]
31. Yang, Y.; Zhang, T.; Le, L.; Ruan, X.; Fang, P.; Pan, C.; Xiong, R.; Shi, J.; Wei, J. Quick and facile preparation of visible light-driven TiO₂ photocatalyst with high absorption and photocatalytic activity. *Sci. Rep.* **2014**, *4*, 7045. [[CrossRef](#)] [[PubMed](#)]